IEEE Access
Multidisciplinary | Rapid Review | Open Access Journal

Received August 2, 2019, accepted August 15, 2019, date of publication August 19, 2019, date of current version August 30, 2019.

Digital Object Identifier 10.1109/ACCESS.2019.2936247

Multi-Source Evidence Data Fusion Approach to Detect Daily Distribution and Coverage of *Ulva Prolifera* in the Yellow Sea, China

ZHONGYUAN WANG[1], ZHIXIANG FANG[1,2], YICHEN WU[1], JIANFENG LIANG[3], AND XIAO SONG[3]

[1]State Key Laboratory of Information Engineering in Surveying, Mapping and Remote Sensing, Wuhan University, Wuhan 430079, China
[2]Collaborative Innovation Center of Geospatial Technology, Wuhan 430079, China
[3]National Marine Data and Information Service, Tianjin 300171, China

Corresponding author: Zhixiang Fang (zxfang@whu.edu.cn)

This work was supported in part by the National key Research and Development Plan under Grant 2017YFC1405302, and in part by the National Natural Science Foundation of China under Grant 41771473 and Grant 41231171.

ABSTRACT *Ulva prolifera* (U. *prolifera*), a seaweed species in the family Ulvaceae, has been causing green tides in the Yellow Sea, China, every year since 2008. This has attracted the attention of the government and the scientific community because of its influence on the region's marine economy and coastal zone environment. Remote sensing, surveillance ships, and airplanes are three common surveillance approaches used by the State Oceanic Administration (SOA) for *U. prolifera* detection in the Yellow Sea. However, improving the accuracy and convenience of daily *U. prolifera* detection by fusing the data from these sources, and obtaining the coverage area and distribution of *U. prolifera* without human intervention, are two challenges that need to be addressed. To this end, this study proposes an improved multi-source evidence fusion method based on Dempster-Shafer evidence theory to detect the distribution and coverage area of *U. prolifera* using data from multiple sources (MODIS images, Sentinel-2A images, and surveillance ship data). This improved approach can handle the conflicts caused by differences in image characteristics and spatial resolutions as well as differences between surveillance ship data and remote sensing data. The capability of the improved method to extract the distribution and coverage area of *U. prolifera* was tested experimentally. The results agree with the reference data supplied by SOA in terms of spatial position and geometry. The fusion of multi-source data demonstrates better results in the detection of *U. prolifera* coverage area and spatial distribution compared with those from individual data sources. The improved approach can be applied to daily and emergent monitoring tasks for U. *prolifera* detection.

INDEX TERMS *Ulva prolifera*, Dempster-Shafer theory, data fusion, coverage, distribution.

I. INTRODUCTION

Since 2008, massive macroalgal blooms (called ''green tide'') caused by *Ulva prolifera* (*U. prolifera*) have occurred every summer in the Yellow Sea, China. These blooms pose a serious threat to coastal areas, owing to their effects on aquaculture, tourism, and maritime transportation [1]–[3]; they have also caused significant economic losses. For example, approximately 16,000 people and 600 boats were involved in cleanup activities in June 2008. Thereafter, the detection, analysis, and prevention of *U. prolifera* outbreaks have attracted much attention from the scientific community and the government [4]–[6]. For instance, preparing a daily detection report on the coverage and distribution of *U. prolifera* is a routine task of the State Oceanic Administration (SOA), China. This report helps the Chinese government and administrators of coastal cities to make appropriate emergency response decisions when these blooms affect economic activities or coastal environments.

Remote sensing (RS), surveillance airplanes and ships are three common surveillance methods to detect *U. prolifera*. When a green tide starts, SOA uses MODIS images to detect *U. prolifera* over a large sea area. Owing to the high observation frequency (i.e., daily observations), MODIS images can cover the entire area that needs to be monitored and delimit *U. prolifera* blooms on a large scale. However, owing to its

The associate editor coordinating the review of this article and approving it for publication was Muhammad Imran.

This work is licensed under a Creative Commons Attribution 4.0 License. For more information, see http://creativecommons.org/licenses/by/4.0/

coarse resolution (250-m) and cloud cover, the *U. prolifera* blooms can be overestimated [1]. To overcome these limitations, high-resolution RS images (i.e., Sentinel images) and Synthetic Aperture Radar (SAR) images are often used to supplement MODIS images, although these images cannot cover the whole area. SOA also uses ocean surveillance ships to detect *U. prolifera* blooms close to the shore and planes to detect blooms further out to sea. The surveillance ships and planes can help to direct the attention of decision makers to the most important *U. prolifera* bloom areas, check the *U. prolifera* growth conditions, and verify the results from RS images [7], [8]. Among these three methods, remote sensing plays an essential role in the detection and prevention of *U. prolifera* [8], [10] owing to its wide coverage and low cost. Surveillance airplanes or unmanned aerial vehicles (UAVs) can detect *U. prolifera* along their flight paths at a relatively higher speed, but these approaches are costly and heavily depend on weather conditions. Surveillance ships can ascertain the existence of *U. prolifera* directly and accurately with a free working trajectory. However, navigation of these ships is closely related to sea surface conditions, and detection over large areas is expensive. Therefore, data from surveillance ships, airplanes, and UAVs are used as auxiliary data in *U. prolifera* monitoring, because of their limited scope or high cost [2], [1], [8].

The resolution, repeat cycle, and availability of RS satellite images are three critical factors that must be considered when selecting a data source for SOA's daily high-frequency detection and accurate mapping of *U. prolifera* distribution and coverage area. Moderate Resolution Imaging Spectroradiometer (MODIS) images (250-meter-resolution), Sentinel-2A images (10-meter-resolution), Synthetic Aperture Radar (SAR) images (10–100-meter-resolution), and Landsat images (30-meter-resolution) are the most popular data sources for detecting green tides [9], [12]–[14]. MODIS (1-day repeat cycle) has a notably higher observation frequency than Landsat (16-day repeat cycle) [15]. The Sentinel series of satellites, with a 10–60 m resolution and a 10-day visit cycle [16], [17], the WorldView series of satellites with a 3.5-meter resolution and a 1.7-day visit cycle on average [16], [18], and the SPOT-6/7 satellites with a 10-meter resolution and a 26-day visit cycle [1], [19] have higher *U. prolifera* detection accuracies than MODIS under normal circumstances. Among these RS data, the MODIS and Sentinel series of satellites are open, free, and easy to acquire and with suitable visit cycle in *U. prolifera* detection. Therefore, this study used Sentinel-2A and MODIS images to implement the proposed method. WorldView images are not widely used in detecting *U. prolifera* blooms because WorldView data is too expensive for the SOA, China. Landsat images are also not chosen as the data source in this study because the long visit cycle (16 days) does not match the requirements of SOA's daily detection.

Some previous studies have focused on identifying the most appropriate satellite images. For example, Cui et al. compared the monitoring ability based on different data sources, including MODIS, the China Small Satellite Constellation for Environment and Disaster Monitoring and Forecasting (HJ-1A/B), Environmental Satellite (EnviSat), and Advanced Synthetic Aperture Radar (ASAR) [20]. An improved method for assessing and refining the satellite-derived massive green macroalgal coverage area with high-resolution images was also proposed [1]. This work compared the *U. prolifera* identification accuracy of MODIS with that of other high-resolution satellites. In short, given high- or moderate-resolution RS data, the low accuracy of low-resolution RS data, and the limited range of surveillance ship data, this study combines these three evidence data types to detect *U. prolifera*, thereby compensating for their individual disadvantages. In this study, MODIS and Sentinel-2A satellite images were chosen as appropriate RS data sources for SOA's high-frequency detection and accurate mapping of *U. prolifera* distribution and coverage area. During green tide events, surveillance ship data and airplane or UAV data will also be included in the task of detection and mapping [1].

Another avenue of research is to use various vegetation indexes, such as the normalized difference vegetation index (NDVI) [9], [21], the ratio vegetation index (RVI) [22], and the enhanced vegetation index (EVI) [23], to detect *U. prolifera*. Of these, NDVI is the most popular index used in the identification of *U. prolifera* [9], [24]; it was improved and applied for the first time by Rouse et al. [25]. Recently, Cao et al. used NDVI calculated from MODIS bands to analyze the patterns and characteristics of [9]. Xiao et al. compared six commonly used vegetation indexes to determine the differences in their sensitivity for *U. prolifera* detection. Using Geostationary Ocean Color Imager (GOCI) data [26], Cai et al. compared and verified the monitoring abilities using NDVI, RVI, the floating algal index (FAI), floating Green Algae for GOCI (IGAG), and normalized difference angular index (NDAI) and proposed an algorithm called NDVI-a that significantly improved the algae detection ability [27]. However, these studies selected or designed only one vegetation index for *U. prolifera* detection, overlooking the advantages of others. (For example, RVI is more sensitive to high-coverage vegetation areas, whereas NDVI is more sensitive to low-coverage vegetation areas [22], [24]. Moreover, it is difficult to directly determine the correctness of a particular vegetation index, because the optical images cannot directly capture a period of *U. prolifera* growth without other information of *U. prolifera*. Therefore, it is necessary to interpret an optical image in a comprehensive context of various vegetation indexes. In other studies, new vegetation indexes were constructed according to the special characteristics of algae. For example Hu proposed an improved version of the floating algal index (FAI) [12]. Although FAI has some advantages in detecting *U. prolifera*, there is still substantial uncertainty with this index, and FAI is more suitable with high-resolution images. Xing and Hu improved the virtual baseline floating macroalgae height (VB-FAH) to monitor *U. prolifera* [3]. Both these indexes are suitable for use with high-resolution images. Currently, there is no

vegetation index suitable for use in *U. prolifera* detection that has good applicability to images from a variety of satellites. Each index has its own strength and weakness. Thus, this study will extract NDVI, FAI, RVI and DVI from MODIS and Sentinel-2A images to make up for the limitations of these indexes in *U. prolifera* detection.

For the detection and surveillance of *U. prolifera*, it is crucial to fuse evidence data from multiple sources in a way that considers both efficiency and accuracy. The conflicts among multiple sources are of three types: (i) conflicts caused by differences of image characteristics, (ii) conflicts between surveillance ship data and RS data, and (iii) conflicts caused by different spatial resolutions. The conflicts of evidence data sources need to be handled well in this task. The D-S evidence theory [28], [29] is often used to solve these conflicts. There are two factors leading to conflicts in data fusion [30], [31] when using D-S evidence theory. One is sensor unreliability due to data limitations and incompleteness of the knowledge of the world; the other is discernment distributions. If the discernment distributions are not consistent, the conflicts will have a considerable influence on the result. There are two main ways to solve these two problems. One is by improving the combination rule, which starts from the original flaws of the evidence synthesis. The most typical method, proposed by Yager [32], assumes that conflicting evidence also carries some useful information that can be assigned to unknown items and used effectively. The other is by modifying the sources of evidence in order to avoid conflicts [33]. This study will use the second approach to fuse data from multiple sources.

This study aimed to answer two questions: how to improve the accuracy and convenience of *U. prolifera* detection by fusing surveillance ship data and various kinds of RS data, and how to obtain the coverage area and distribution of *U. prolifera* automatically without human intervention. To answer these two questions, this study proposes an improved multi-source evidence fusion method based on Dempster-Shafer (D-S) evidence theory to detect the distribution and coverage area of *U. prolifera* in the Yellow Sea using data from multiple sources. The improvement could be summarized into three parts. (i) The evidences in original sources are sorted in descending order of the support matrix value of evidences, and the first half of the evidences are selected as the new source. This support matrix value is used to filter evidences with large conflicts with others. (ii) The evidences in the second half in the original source, which has a high characteristic grade defined by this study, are also selected as the new source. The characteristic grade aims to keep the important evidences from original sources. (iii) The compatibility matrix is included in the evidence's basic probability assignment (BPA) in D-S theory according to the characteristic grade and the compatibility between items of evidence, which could balance the conflict of evidences in the new source (characteristics of original sources). After extraction of the coverage area of *U. prolifera*, this study designs an algorithm to automatically generate the distribution range for *U. prolifera* based on five indexes (number of pattern spots, area, perimeter, shape index, and patch density). This paper makes two main contributions. The first is to propose an improved multi-source evidence fusion method of *U. prolifera* detection by fusing several vegetation indexes using various kinds of available optical images and surveillance ship data. The second is to propose a comprehensive solution for conflicts arising in the fusion of data (Sentinel-2A, MODIS, and surveillance ship data) related to *U. prolifera*.

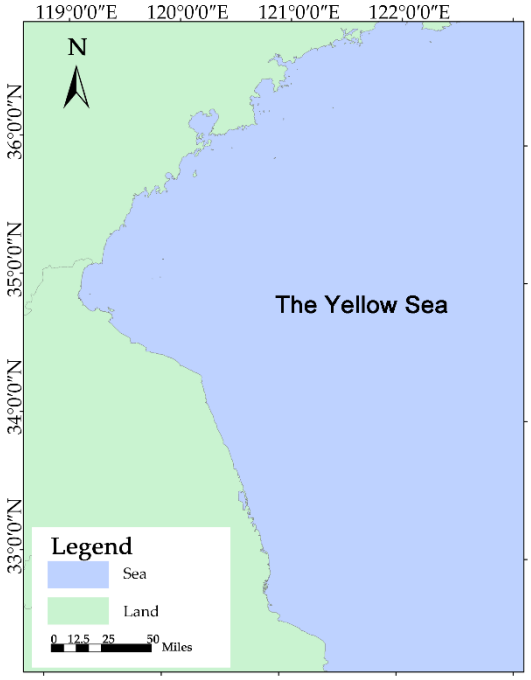


FIGURE 1. Map of the study area.

The paper is divided into four parts. Section 2 provides details of the method of detecting U. *prolifera* by fusing MODIS images, Sentinel-2A images, and surveillance ship data. Section 3 provides the results and analysis. Section 4 presents conclusions and discusses key points for future research.

II. MATERIALS AND METHODS

A. STUDY AREA

The Yellow Sea is located between China and Korea. It connects to the Bohai Sea on the north and is separated from the western Pacific Ocean by the East China Sea to the south. Owing to the monsoon, the Yellow Sea is cold and dry in winter and warm and humid in summer. The salinity of seawater is about 33%, and the annual variation in water temperature is 13–24°C, which is suitable for the development of algal blooms. Green tides have occurred here regularly for the past ten years. The study area extended from 120°E to 123°E and from 33°N to 37°N in the southern Yellow Sea (Fig. 1), which has experienced green tide outbreaks of green tide for ten years.

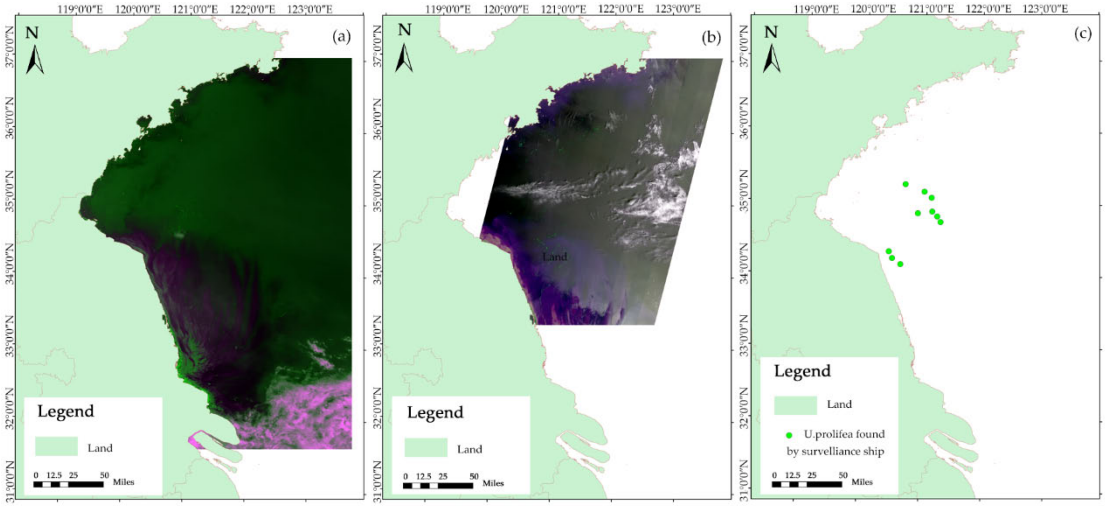


FIGURE 2. Experimental data: (a), (b), and (c) show the moderate resolution imaging spectroradiometer (MODIS) data, Sentinel-2A data, and surveillance ship data, respectively, for the yellow sea on June 3, 2018. The green dots in (c) refer to the location of *U.* prolifera found by surveillance ships.

B. DATA

This study used MODIS and Sentinel-2A image data to detect the *U. prolifera*. Then, surveillance ship data was used to implement the proposed data fusion approach to detect the distribution and coverage of *U. prolifera* in the Yellow Sea, China.

MODIS is a remote sensing instrument in space that was developed and manufactured by NASA. The instrument can receive data in 36 spectral bands ranging from 0.4 μm to 14.4 μm, including visible and infrared bands. The resolution of the images ranges from 250 m to 1 km, and the earth's surface can be completely scanned at intervals of 1 to 2 days. The images provide a wide variety of global data, including changes in cloud cover, surface radiation energy, and ocean and land processes. Of these, the 20-meter-resolution images cover the red band, near-infrared bands, and short-wave infrared band resampled from 500-meter-resolution products. These characteristics of MODIS can be used to detect *U. prolifera*.

Sentinel-2A, a satellite launched by the European Space Agency (ESA), is a 290-kilometer-wide satellite. It can completely scan the earth's surface every 10 days. Its Multispectral Instrument (MSI) covers 13 bands, including visible light bands, near-infrared bands, and the short-wave infrared band. The resolution for each band ranges from 10 m to 60 m. The red and near-infrared bands have a resolution of 10 m, and the short-wave infrared band has a resolution of 20 m. Of the optical data, data from the satellites Sentinel-2A and -2B are the only data with three bands in the red-edge range, which is particularly effective for monitoring *U. prolifera*. Daily surveillance ship data is sparse. Combining only surveillance ship and MODIS images may not improve the accuracy of the *U. prolifera* coverage. The resolution of Sentinel-2A is 10 m and its visit cycle is 10 days, which means that Sentinel-2A may cover only part of the study area but with high resolution. This is why Sentinel-2A data was chosen in this study.

Due to the different resolutions of MODIS and Sentinel-2A, MODIS images are resampled to 10 m for the data fusion approach, which aims to keep the details of images to improve the accuracy of *U. prolifera* detection. The resampling approach used here is the Cubic Convolution approach, which has better performance with less aliasing and blurring in the quality of images than the nearest neighbor and bilinear interpolation [34]. The three approaches above are the most adopted methods in image resampling. If the Sentinel-2A data are resampled to 250 m, many details will be lost, and the data fusion results of *U. prolifera* from Sentinel-2A and MODIS will be enlarged.

Besides the RS images, surveillance ships will also be used in *U. prolifera* detection. The surveillance ship data could provide accurate information of *U. prolifera* for a small area (Fig. 2c) and can verify the results from RS images [7], [8]. However, because of the limitations in staffing and financial resources, surveillance ship data cannot provide continuous monitoring over a wide area, but is only an auxiliary means for *U. prolifera* detection.

C. METHODS

Fig. 3 outlines the improved method proposed in this study. The work is divided into three steps: (i) extraction of vegetation indexes from remote sensing images, (ii) Gaussian mixture model (GMM) fuzzy classification for classifying the *U. prolifera* and sea water, (iii) data fusion for detecting *U. prolifera*. The following sections will introduce the first step and the third step in detail. In the second step, this study used fuzzy classification for *U. prolifera* and sea water by employing the GMM [35] based on vegetation indexes in the first step with the number of classification centers as 2. GMM was chosen because of its powerful ability to

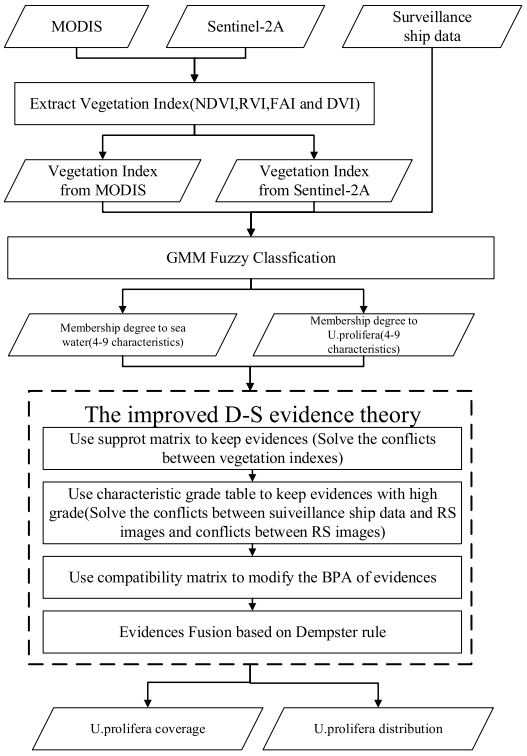


FIGURE 3. Flow chart of the improved method.

provide a smooth overall distribution fit of arbitrarily shaped densities [36]. After using the GMM fuzzy classification, each pixel of characteristics extracted in the first step can be determined between two Gaussian components (i.e. *U. prolifera* and sea water). The membership degree of the same pixel for different characteristics may be different, and data fusion is needed to acquire an appropriate result. If there is only water in the sea, the membership degree of *U. prolifera* in each characteristic will be 0. This will not affect the following steps.

There are three conflicts after fuzzy classification (conflicts between RS images and surveillance data, conflicts between RS images, and conflicts between vegetation indexes). To resolve the conflicts between vegetation indexes, this study improves D-S evidence theory by using a support matrix to retain the evidence with high support and remove the evidence with high conflicts due to the vegetation indexes. To solve the conflicts between RS images and surveillance ship and conflicts between RS images, the study improves the D-S evidence theory by using a characteristic grade table to add the evidence with high grade (i.e., surveillance ship data) to the data fusion. After GMM fuzzy classification, the membership degree to *U. prolifera* and sea water of each characteristics at each pixel will be used as BPA and each characteristic will be used as evidence in the improved D-S evidence. In the improved D-S evidence, this study first calculated the support matrix, which describes the support between each pair of evidence. This study sorted the evidences in descending order according to the support and included the first half of the evidences into the data fusion. Second, this study designed a characteristic grade table to include the surveillance ship data and Sentinel-2A data into the data fusion. After selecting the evidences into data fusion, this study used a compatibility matrix to modify the BPA of each evidence according to the credit of each pixel. In the end, this study used the Dempster-rule to fuse these evidences and obtained a reasonable *U. prolifera* coverage.

After extracting the coverage and distribution of *U. prolifera*, the results from are analyzed from the perspective of position and geometry, which will be described in Section III.

1) EXTRACTING VEGETATION INDEXES FROM RS DATA

Using optical images to monitor *U. prolifera* is based on the difference in spectral characteristics between the sea surface and the sea surface covered by *U. prolifera*. When covered with *U. prolifera,* which is rich in chlorophyll, the sea surface will produce an absorption valley in the blue and red bands of visible light and a reflection peak in the near-infrared band [20], [12]. A thicker coverage of *U. prolifera* will result in a more obvious reflection peak.

NDVI, RVI, DVI, and FAI, which are commonly used indexes, can be constructed using the red band, the near-infrared band, and the short-wave infrared band of MODIS and Sentinel-2A. NDVI may be the most commonly used index for detecting U. *prolifera* in sea areas [9]. NDVI has higher sensitivity in low vegetation coverage than in high vegetation coverage, so it is suitable for early and mid-term *U. prolifera* detection [22]. On the other hand, RVI has higher sensitivity in high vegetation than in low vegetation, and is suitable for late detection of *U. prolifera*. DVI is the vegetation index that is most sensitive to the difference between *U. prolifera* and seawater. Hu pointed out that NDVI, RVI, and DVI yield uncertain results when describing algae and went on to construct the FAI, which has a strong ability to detect algae in optical images with high resolution [12]. In summary, the four vegetation indexes selected have irreplaceable advantages in detecting *U. prolifera.* The formulas of the four vegetation indexes are as follows:

$$\mathrm{NDVI} = \frac{NIR - RED}{NIR + RED} \tag{1}$$

$$\mathrm{RVI} = \frac{NIR}{RED} \tag{2}$$

$$\mathrm{DVI} = NIR - RED \tag{3}$$

$$\mathrm{FAI} = NIR - (RED + (SWIR - RED) \times \frac{\lambda_{\mathrm{NIR}} - \lambda_{\mathrm{RED}}}{\lambda_{\mathrm{SWIR}} - \lambda_{\mathrm{RED}}}) \tag{4}$$

In (1)–(4), NIR, RED, and SWIR represent the observed reflectance of the near-infrared band, red band and the short-wave infrared band, respectively. λ_{NIR} and λ_{RED} represent the wavelengths of near-infrared and red bands, respectively. NIR, RED, and SWIR bands are 841–876-nm, 620–670-nm, and 1628–1652-nm for AQUA MODIS (250-m spatial resolution). λ_{NIR}, λ_{RED}, and λ_{SWIR} are 859-nm, 645-nm, and 1240-nm [12] for AQUA MODIS

(250-m spatial resolution). The band numbers of NIR, RED, and SWIR bands from Sentinel-2A are B8, B4, and B11 Sentinel-2A (10-m spatial resolution). λ_{NIR}, λ_{RED}, and λ_{SWIR} are 842-nm, 665nm, and 1610-nm.

2) IMPROVED APPROACH FOR U. PROLIFERA DETECTION

After the data set is pre-processed, nine classes of characteristics are prepared; namely, the surveillance ship data and four characteristics (NDVI, DVI, RVI, and FAI) in corresponding MODIS and Sentinel-2A data. Each pixel in RS images corresponds to 4–9 classes of characteristics due to the coverage scenarios of remote images. For example, if a location is only covered by MODIS, it has only 4 characteristics (NDVI, DVI, RVI, and FAI). If a location is covered by MODIS, Sentinel-2A and the surveillance ship data, it has nine classes of characteristics. In our study, there are two components (sea water, *U. prolifera*) and each pixel corresponds to 4-9 characteristics. However, these characteristics may conflict at certain locations, as described above. This study proposes a data fusion approach to detect *U. prolifera* by extending the D-S evidence theory [28], [29]. Before introducing the approach, this study concludes the conflicts existing in pre-processed data, as follows:

Conflict 1: Conflicts caused by differences in image characteristics.

As stated in Section 2.3.1, different vegetation indexes extracted from the same optical image, even when describing the same type of feature, will have different values. This difference in characteristics is a cause of conflicts.

Conflict 2: Conflicts between surveillance ship data and RS data.

MODIS data and Sentinel-2A data are not as accurate as surveillance ship data, because optical images are obtained by remote detection. The use of different detection methods can lead to massive data conflicts in the fusion process.

Conflict 3: Conflicts caused by spatial resolution

In order to fuse the Sentinel-2A data with the MODIS data and not disregard the information obtained by Sentinel-2A, it is necessary to resample MODIS data to the resolution of Sentinel-2A in the region where there is Sentinel-2A data. Because of its original low resolution, MODIS data may be missing some details. Thus, differences in spatial resolution are another cause of conflicts.

To resolve these three kinds of conflict, this paper presents an improvement to the D-S evidence theory, which includes three aspects:

(i) Constructing a support matrix to keep evidences with a high support degree

The higher support degree of evidences in D-S theory means they have a lower degree of conflict. To prevent these conflicts, it is necessary to keep the evidences with high support degree. The support degree between pairwise items of evidence can be calculated using the Belief Jensen–Shannon (BJS) index [37]. The BJS integrates the Dempster–Shafer evidence theory with Jensen–Shannon divergence, and is able to measure the discrepancy and conflict degree between the evidences. BJS between evidences m_1 and m_2 is defined as follows:

$$\begin{aligned} \mathrm{BJS}(m_1, m_2) &= H\left(\frac{m_1+m_2}{2}\right) - \frac{1}{2}Ht(m_1) - \frac{1}{2}H(m_2) \\ &= \frac{1}{2}\left[\sum_i m_1(A_i)\log\left(\frac{2m_1(A_i)}{m_1(A_i)+m_2(A_i)}\right)\right. \\ &\quad \left. + \sum_i m_2(A_i)\log\left(\frac{2m_2(A_i)}{m_1(A_i)+m_2(A_i)}\right)\right] \end{aligned} \quad (5)$$

where $\mathrm{BJS}(m_1, m_2) \in [0, 1]$, $H(m_j)$ is the Shannon entropy, A_i is the i^{th} component of GMM results, namely, *U. prolifera*($i = 1$) or sea water ($i = 2$). $m_j(A_i)$ is the membership degree to the i^{th} component of the j^{th} characteristic within 4-9 characteristics of each pixel after GMM fuzzy classification.

Then, the support matrix of evidences can be formulated as follows:

$$\mathrm{SM} = \begin{bmatrix} 0 & \cdots & 1-BJS_{1i} & \cdots & 1-BJS_{1k} \\ \vdots & \cdots & \vdots & \cdots & \vdots \\ 1-BJS_{i1} & \cdots & 0 & \cdots & 1-BJS_{ik} \\ \vdots & \cdots & \vdots & \cdots & \vdots \\ 1-BJS_{k1} & \cdots & 1-BJS_{ki} & \cdots & 0 \end{bmatrix} \quad (6)$$

where k is the number of evidences. SM represents all support degrees of mutual evidences. This study calculates the sum of the support degree for each item of evidence as follows:

$$Sup_j = \sum_{m=1}^{k} \mathrm{SM(m, j)} \quad (7)$$

where Sup_j is used to indicate the capability of evidence j in supporting other evidences. Then, Sup_j is sorted in descending order, and the first half of the evidences is selected as a set of evidence called *Source*, which will be used in the improved approach. Therefore, the support matrix approach can retain evidence with a high support degree and remove the evidence with large conflicts.

(ii) Constructing a characteristic grade table to retain the important evidences

Using the support matrix, the surveillance ship data and Sentinel-2A data are possible to be removed from *Source*. However, the surveillance ship data is more reliable than the Sentinel-2A data. The Sentinel-2A data has a high possibility of being more reliable than the MODIS data. To retain the important evidences in *Source*, this study constructs a characteristic grade table (Table 1), in which the nine characteristics involved in the future fusion are divided into five levels. Specifically, the surveillance ship data has the highest grade rating of 1. NDVI and FAI are most widely used in *U. prolifera* extraction, and the accuracy of Sentinel-2A is higher than that of MODIS. Kumar et al. compared the NDVI, DVI, and RVI based on density, biomass, and Shannon's and Simpson's indices, and found that NDVI is better than DVI and RVI [38]. Hu found that FAI has advantages over

TABLE 1. Characteristic grade table constructed in this study.

Characteristic	Grade rating
Surveillance ship data	1
NDVI (Sentinel-2A), FAI (Sentinel-2A)	2
NDVI (MODIS), FAI (MODIS)	3
DVI (Sentinel-2A), RVI (Sentinel-2A)	4
DVI (MODIS), RVI (MODIS)	5

NDVI because FAI is less sensitive to changes in environmental and observation conditions (aerosol type and thickness, solar/viewing geometry, and sun glint) and can ''see'' through thin clouds [12]. Thus, the NDVI and FAI derived from Sentinel-2A images are rated as 2, and the NDVI and FAI derived from MODIS images are rated as 3. The RVI and DVI extracted from Sentinel-2A are rated 4, whereas the RVI and DVI extracted from MODIS are rated 5. Table 1 shows the characteristic grade table constructed in the study.

After establishing the characteristic grade table, this study also adds suitable characteristics j to *Source* from the second half of the evidences that have been sorted according to support degree in the previous step, if characteristic j meets Conditions (a), (b), and (c) simultaneously:

Condition (a). $Characteristic_j \notin Source$

Condition (b). $\exists Characteristic_c \in Source, grade_c < grade_j$

Condition (c). $\forall grade_c = grade_j, c \notin Source$

where $Characteristic_c$ is the characteristic in *Source* and $Characteristic_j$ is the j^{th} characteristic within 4-9 characteristics of each pixel after GMM fuzzy classification; $grade_c$ and $grade_j$ denote the grade rate of $Characteristic_c$ and $Characteristic_j$, respectively, in the characteristic grade table; $grade_c$ and $grade_i$ denote the grades of characteristic c and characteristic i, respectively.

This step is performed to ensure that the high grade characteristics will be selected for addition to *Source*. Although items of evidence with high grade may be added to *Source* by the characteristic grade table, such items may or may not have a high support degree.

(iii) Constructing a compatibility matrix to balance the conflict of evidences.

After using the characteristic grade table, the evidences in *Source* may not all have a high support degree. Therefore, $m_j(A_i)$, the GMM classification result, is not suitable and is therefore not directly used as BPA in D-S evidence theory. It is necessary to modify $m_j(A_i)$ before use as BPA in D-S theory according to the compatibility between items of evidence. This study constructs a compatibility matrix [39] to calculate the total compatibility of each piece of evidence about A_i in *Source*. Then, the total compatibility is used to modify $m_j(A_i)$ to resolve the problem of fusing the highly conflicting evidences.

The compatibility ratio (R) is an index describing the compatibility and conflict between two evidences. It is defined as:

$$R_{p,q} = \frac{2m_p(A_i)m_q(A_i)}{m_p(A_i)^2 + m_q(A_i)^2} \tag{8}$$

where $m_p(A_i)$ and $m_q(A_i)$ are the membership degree to A_i of two evidences in *Source* and p and q denote the id's of the evidences in *Source*.

The compatibility matrix represents all mutual compatibility ratios in *Source* about A_i, namely, *U. prolifera*($i = 1$) or sea water ($i = 2$). The compatibility matrix can be calculated using (8) and (9).

$$R(A_i) = \begin{bmatrix} R_{1,1} & R_{1,2} & \cdots & R_{1,n} \\ R_{2,1} & R_{2,2} & \cdots & R_{2,n} \\ \vdots & \vdots & \ddots & \vdots \\ R_{n,1} & R_{n,2} & \cdots & R_{n,n} \end{bmatrix} \tag{9}$$

where n is the number of evidences in *Source*.

Then, the absolute compatibility of each piece of evidence about A_i in *Source* can be calculated based on Eq. 10, and this paper modified the $m_p(A_i)$ of the evidence items by using the degree of compatibility according to Eq. 11.

$$D_p(A_i) = \sum_{p=1,q\neq j}^{n} R_{p,q}(A_i) \tag{10}$$

$$m_p(A_i)' = \frac{D_p(A_i)}{(n-1)} m_p(A_i) \tag{11}$$

Based on the above modifications, the D-S evidence theory (Dempster, 1967; Shafer 1976,) could be extended to detect *U. prolifera* by fusing the MODIS, Sentinel-2A, and surveillance ship data. θ represents the evidences (i.e.*Source*) in D-S evidence theory, which can be understood as all basic values of the evidences. The basic probability assignment function m: $2^m \rightarrow [0, 1]$ and satisfies the following conditions: the mass of the empty set m $(\emptyset) = 0$, and $\sum_{A\in\theta} m(A)' = 1$. For a case with multiple sources of evidence, the BPAs can be combined to yield a new BPA function, M, which is defined as follows according to Dempster's rule:

$$\begin{aligned} &\mathrm{M}(\mathrm{A}) \\ &\quad = \begin{cases} \dfrac{1}{K} \displaystyle\sum_{A_1\cap A_2\cap\ldots\cap A_n=A} m_1(A_1)' m_2(A_2)' \ldots m_n(A_n)', \\ \qquad A = \emptyset \\ 0, \qquad A \neq, \emptyset \end{cases} \\ &K = \sum_{A_1\cap A_2\cap\ldots\cap A_n\neq\emptyset} m_1(A_1)' m_2(A_2)' \ldots m_n(A_n)' \\ &\quad = 1 - \sum_{A_1\cap A_2\cap\ldots\cap A_n=\emptyset} m_1(A_1)' m_2(A_2)' \ldots m_n(A_n)' \end{aligned} \tag{12}$$

where K is a normalization constant, m_i' is the BPA of evidence item i.

After modifying the BPAs of selected items of evidence, the evidence items in *Source* can be fused by the Dempster combination rule, and the corresponding probabilities in the pixel for every type of ground object are obtained. In this way, images with probabilities in each pixel for all ground object types (which in this study are *U. prolifera* and seawater)

are obtained. The interpreter can set the allowable threshold of probability according to the extraction requirement (Fig. 5a). Thus, using this method, it is possible to compare the probabilities of corresponding pixels in different images and choose the largest one as the feature class for that pixel. The collection of pixels, whose feature class is *U. prolifera,* is called as *U. prolifera* coverage area.

3) FINDING THE DISTRIBUTION AREA OF U. PROLIFERA

The distribution area, which can also be called the influence area, aggregates scattered fragments of the *U. prolifera* coverage area into relatively large fragmented areas, including all of the patches and the region among the adjacent patches. The distribution area of *U. prolifera* is a different index from its coverage area. Both these indexes are commonly used by North China Sea Marine Forecasting Center of State Oceanic Administration. The general approach of the distribution area includes setting an inner buffer zone or manually drawing the boundary of the *U. prolifera* distribution. These two methods have limitations in terms of their unknown suitable buffer distance and the significant amount of manual drawing effort involved.

Therefore, this study designs an algorithm to generate the distribution range for *U. prolifera* automatically. The designed algorithm aims to find the whole outlier in geographical space. The method is divided into two steps. The first step calculates all of the polygons under a specified threshold for possible distances, which is described as follows:

(i) Set the initial threshold $d = cellsize$, where *cellsize* is the pixel size.

(ii) Take an unselected point F in the *U. prolifera* coverage area as the initial point and mark that point as selected.

(iii) Using the idea of the Moore neighborhood tracking algorithm [40], search from F to the right for $d/cellsize$ units, and explore from F downward for $d/cellsize$ units. If a point of *U. prolifera* coverage is encountered, stop, and select the points in the path.

(iv) Repeat Steps (ii)–(iii) until all points in the coverage area are selected. Record the polygon formed by this series of iterations.

(v) Let $d = d+cellsize$, and repeat Steps (ii)–(iv), stopping when the number of polygons formed is 1.

If d is small, the number and the fragmentation of the *U. prolifera* distribution will be larger and vice versa. So, the second step determines the best polygon by using five indexes: number, area, perimeter, patch density, and shape index. These five indexes can be used to describe the number and fragmentation of the *U. prolifera* with different values of d. Number (N) denotes the number of polygons covering the *U. prolifera*. Area (S) denotes the total area of all the polygons. Perimeter (C) denotes the total perimeter of all the polygons. N, S, and C are used to describe the scale of the *U. prolifera* distribution. The small N and large S and C mean that the result may overestimate the *U. prolifera* distribution and vice versa. The patch density (Pd) [41] , [42] is the ratio of the number to the area, which can describe the degree of fragmentation. The shape index (Si) is the degree of similarity between the pattern and a square [43]. Pd and Si are two indexes used to describe the fragmentation of *U. prolifera* distribution. Large Pd and Si values mean that the *U. prolifera* distribution is fragmented, and small Pd and Si values mean that it is not.

TABLE 2. Equations for calculating five indexes.

Index	Meaning	Equation
N	Number of *U. prolifera* distribution polygons	
C	Total perimeter of *U. prolifera* distribution polygons	$C = \sum_{i}^{N} c_i$ where c_i is the perimeter of polygon i
S	Total area of polygons *U. prolifera* distribution polygons	$S = \sum_{i}^{N} s_i$ where s_i is the area of polygon i
Si	Shape index of *U. prolifera* polygons	$Si = \frac{0.25C}{S}$
Pd	Patch density of *U. prolifera* polygons	$Pd = \frac{N}{S}$

The equations for calculating the five indexes are shown in Table 2.

Fig. 4 shows the *U. prolifera* distribution when d = 2500 m, 7750 m, and 25000 m. The N values of Fig. 4a, Fig. 4b, and Fig. 4c are 265, 21, and 4, respectively. The C values of Fig. 4a, Fig. 4b, and Fig. 4c are 5200.50 km, 4065.25 km, and 2082.50 km, respectively. The S of Fig. 4a, Fig. 4b, and Fig. 4c are 5291.75 km^2, 18332.50 km^2, and 39443.25 km^2, respectively. From the perspective of N, S, and C, the *U. prolifera* distribution in Fig. 4a is too small, and that in Fig. 4c is too large. The Pd values of Fig. 4a, Fig. 4b, and Fig. 4c are 3.13×10^{-3}, 7.16×10^{-5}, and 6.34×10^{-6}, respectively. The Si values of Fig. 4a, Fig. 4b, and Fig. 4c are 0.06142, 0.01385, and 0.00330, respectively. From the perspective of Pd and Si, Fig. 4b is more suitable to describe the *U. prolifera* distribution compared with Fig. 4a and Fig. 4c.

This study calculates the five indexes of the polygon for each iteration in Step 1 and sorts them according to the distance threshold. Then, the rates of change for the five indexes could be calculated as follows:

$$rate_{index,i} = \frac{\frac{index_i - index_{i+1}}{d_i - d_{i+1}} - \frac{index_{i+1} - index_{i+2}}{d_{i+1} - d_{i+2}}}{d_i - d_{i+2}} \quad (13)$$

where i denotes the number of the iteration and *index* denotes one of the five indexes in Table 2. This study ends the iteration of determining the polygon if these five indexes converged and show very small differences (e.g., less than 1%).

III. RESULTS AND ASSESSMENTS

A. RESULTS AND PARAMETER DETERMINATION

The results of this study show the coverage and distribution areas of *U. prolifera*. Fig. 5 compares the indexes

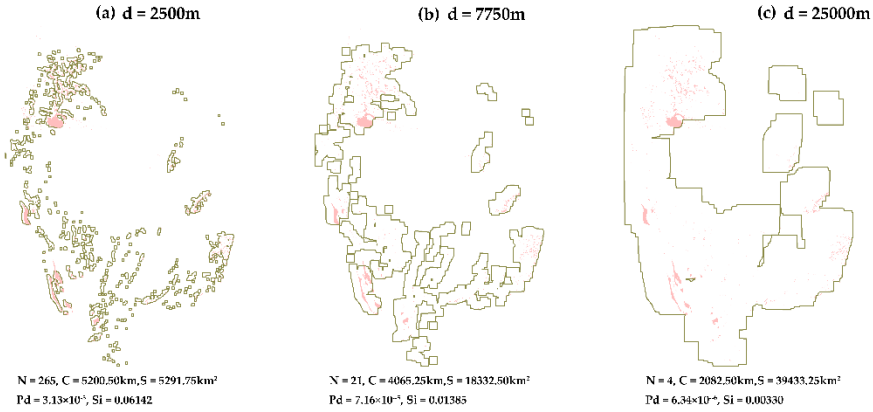


FIGURE 4. Distribution of *U. prolifera* for d = 2500 m, d = 7750 m, and d = 25000 m.

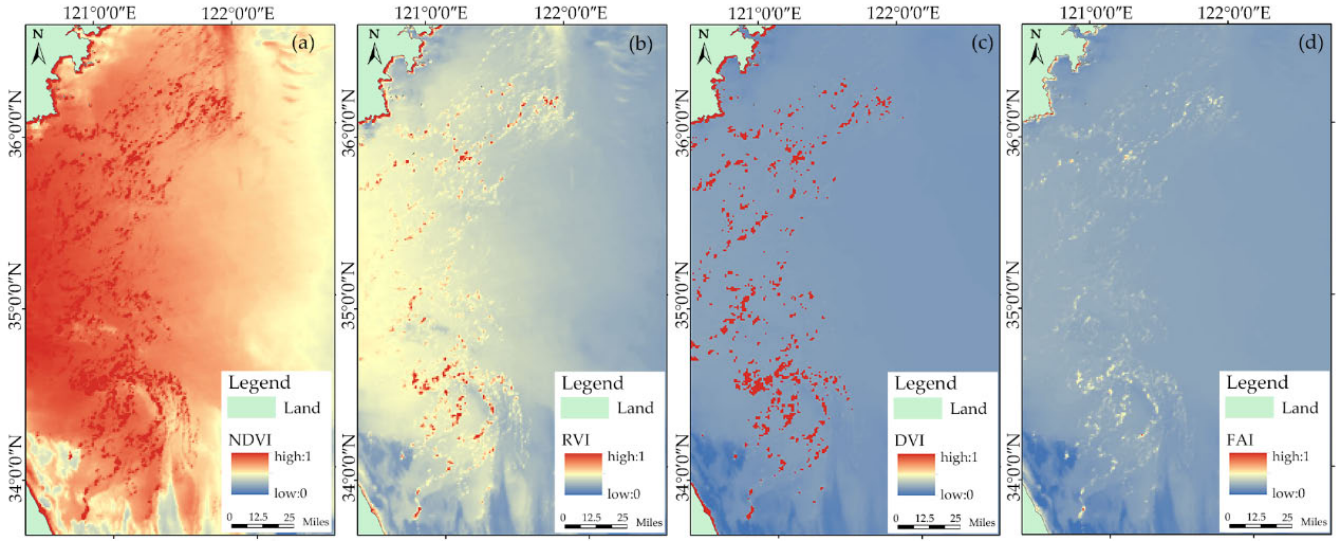


FIGURE 5. Comparison of the four vegetation indexes: (a), (b), (c), and (d) show the normalized difference vegetation index (NDVI), ratio vegetation index (RVI), difference vegetation index (DVI), and floating algal index (FAI), respectively, extracted from the AQUA MODIS data for june 3, 2018. To easily compare them, this paper normalized them all to [−1, 1].

extracted from the MODIS image captured on June 3, 2018, when U. *prolifera* was in its early growth stage [1]. This accounts for the fact that *U. prolifera* is more clearly evident from NDVI (Fig. 5a) than from FAI (Fig. 5b) or RVI (Fig. 5d). The boundaries of the *U. prolifera* bloom region can clearly be seen from the DVI (Fig. 5c). Fig. 6 shows the results of applying the fusion method. Fig. 6a shows the probability of *U. prolifera* presence in a pixel of the images, while Fig. 6b shows the *U. prolifera* coverage area in the Yellow Sea on June 3, 2018: 82.5625km^2. This value does not agree with the coverage area extracted by Cao *et al.* [9]: 365km^2 This could be because of the low resolution of MODIS data; many pixels in the MODIS image are not completely occupied by the green tide, and in the results by Cao *et al.* [9], for any pixel that contains even a little *U. prolifera*, the area of the whole pixel is included in the calculation. This conclusion can also be confirmed by Cui *et al.* [1].

In the improved approach, only the parameter d needs to be determined while calculating the *U. prolifera* distribution area. Fig. 7 shows the rates of change in of the five indexes for different distribution range d values on June 3, 2018. For the conditional termination of iterations for determining d, this study found that the appropriate value of d is 7750 m. The distribution thus obtained is shown in Fig. 8a.

B. ASSESSING THE ACCURACY OF THE RESULTS IN TERMS OF SPATIAL POSITION

To assess the reliability of the extracted results, we compared our results (Fig. 8a) with a digitized map of *U. prolifera* distribution in the Yellow Sea for June 3, 2018, from the SOA (Fig. 8b). Fig. 8b is a reference map that was manually created by the experts of the SOA according to images from MODIS, ENVISAT, RADARSAT1/2-SAR, and COSMO-1/2-SAR, whose coverage area is 98 km^2 and distribution

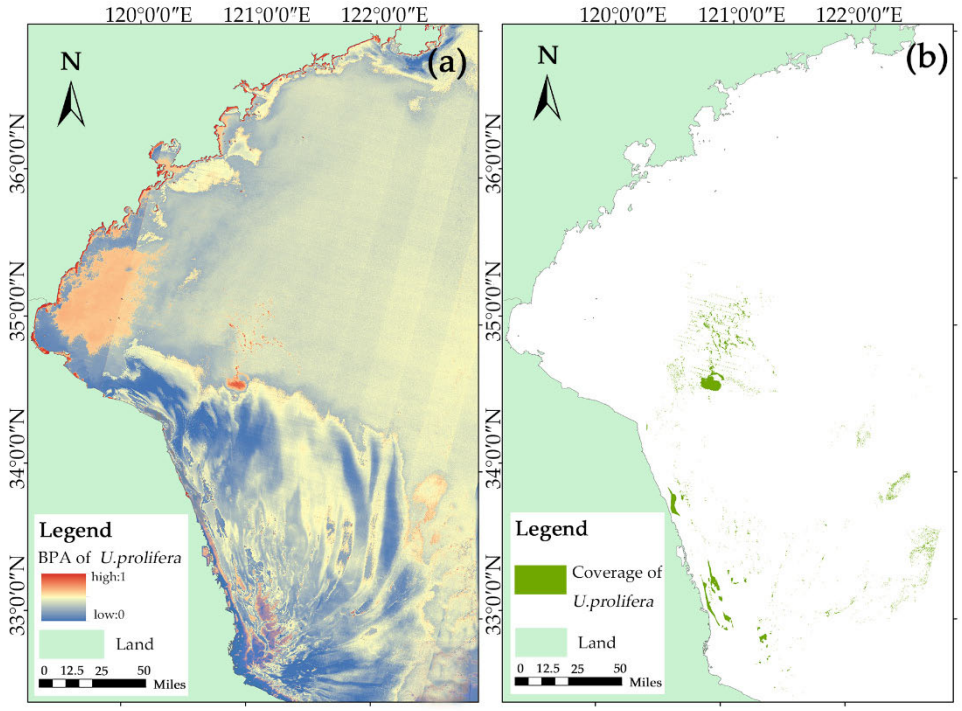


FIGURE 6. Fusion results: (a) shows the probability of *U. prolifera* presence in a pixel and (b) shows the coverage area of *U. prolifera*.

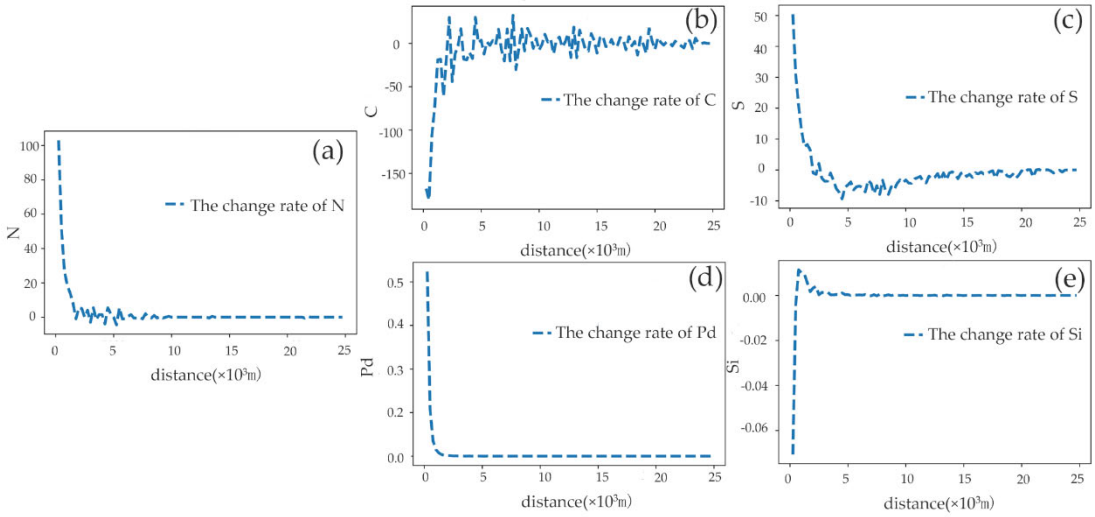


FIGURE 7. The rates in terms of the five indexes for distribution range *d* on June 3, 2018: (a)-(e) show the number N, perimeter C, area S, patch density Pd, and shape index Si, respectively, by distribution range.

range is 28,845km^2. The coverage area in Fig. 8b is slightly larger than that obtained using our improved approach. This is because our improved approach generates outliers of *U. prolifera* distribution areas in the shape of an indentation, while the boundaries in the reference map are smoother than those obtained in this study.

In the reference map, the offshore *U. prolifera* distributions nearest to land are from Xiangshui to Dongtai. The farthest offshore distribution is close to 33°30′ N, 123°E. The southernmost tip of the reference distribution is the area near Rudong. The northernmost distribution in the reference data is close to 35°N, 120°45′ E.

In our map as well, the offshore *U. prolifera* distributions nearest to land are from Xiangshui to Dongtai; the farthest offshore distribution is close to 33°30′ N, 123°45′ E; and the southernmost point of the distribution is a little north of

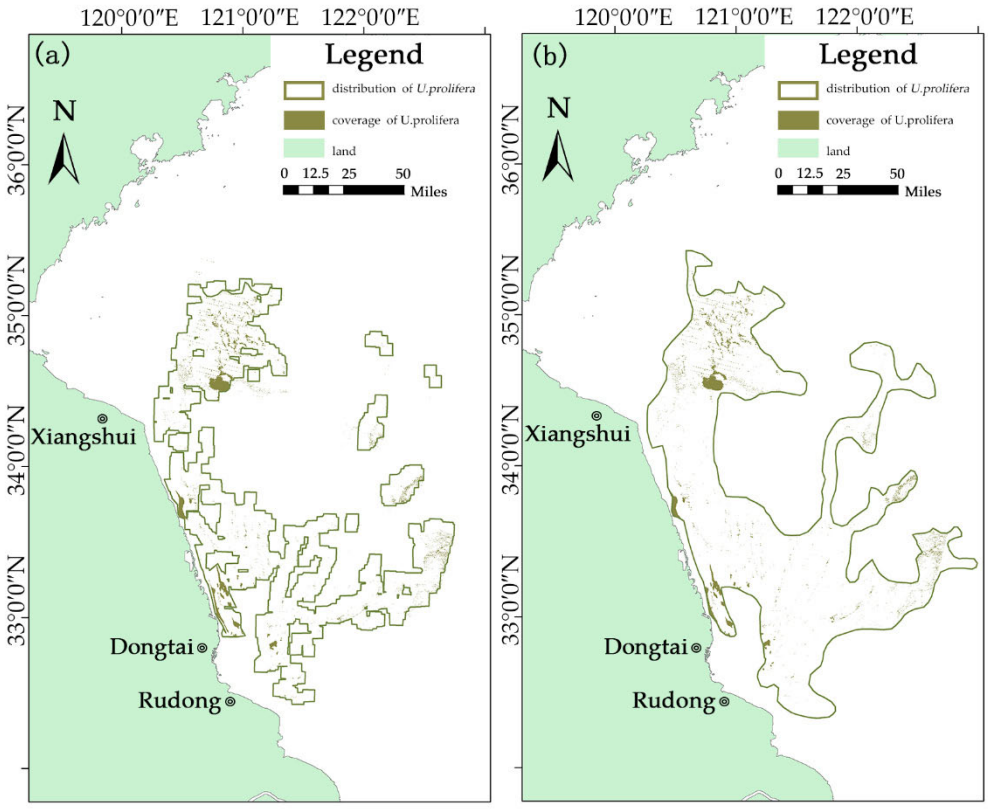


FIGURE 8. Experimental result and reference data: (a) shows the results of extraction by our improved method and (b) shows the reference map drafted by the SOA.

Rudong. Thus, our experimental results are consistent with the reference data. However, the northernmost point of the distribution, according to our extraction results, is 35°25′ 11′′ N, 121°14′ 17′′ E, which is considerably different from that in the reference data. However, we found that the surveillance ship could clearly detect the *U. prolifera* at this location.

The total areas of the distribution in our results and in the reference data are about 26,440 km^2 and 28,845 km^2, respectively. In our results, the total area of the patch overlapping the reference data is 16,887 km^2, accounting for 63.87% of our total area. There is a difference of 5708 km^2 between the results of the surveillance ship detection and the reference data in the north, accounting for 21.86% of our total area. Thus, the accuracy of the results extracted by the improved method is 85.73%. The main reason for this difference is that the reference map was manually drawn; the accuracy would be higher if this factor were disregarded. In summary, the experimental results are correct in terms of spatial position.

C. ASSESSING THE ACCURACY OF THE RESULTS IN TERMS OF GEOMETRY

This study also evaluated the geometry of the results. A standard deviational ellipse is a tool commonly used to define geometric shape and can be easily obtained using ArcGIS 10.2 [9]. This study compared the standard deviational ellipses of the experimental results and those of the reference data (Fig. 9). Measured by standard deviational ellipse, the mean center of the reference data is at 33.83°N, 121.42°E and the mean center of the experimental results is at 33.70°N, 121.47°E. The orientation of the ellipse of the reference data is 158.88°, and that of the ellipse for our results is 158.91°. These two morphological indicators do not the difference between the two distributions clearly, because the difference between the mean centers is 15,772.70 m and the difference between the ellipse orientations is 0.02°. The differences between the long axes and the short axes, however, are notable. By comparing the coverage area of the reference map with that derived using the improved method, it can easily be seen that here as well, the difference is due to the lack of surveillance ship data in the reference data.

D. COMPARING OUR EXPERIMENTAL RESULTS WITH THOSE OBTAINED USING ONLY ONE SOURCE

To illustrate the advantages of using multi-source data, this study compared the results of the introduced methods with those only extracted from Sentinel-2A or MODIS images. Fig. 10 shows the results extracted from only MODIS (Fig. 10a) images, those obtained from only Sentinel-2A images (Fig. 10b) and those obtained by the improved method in this paper (Fig. 10c) for June 3, 2018.

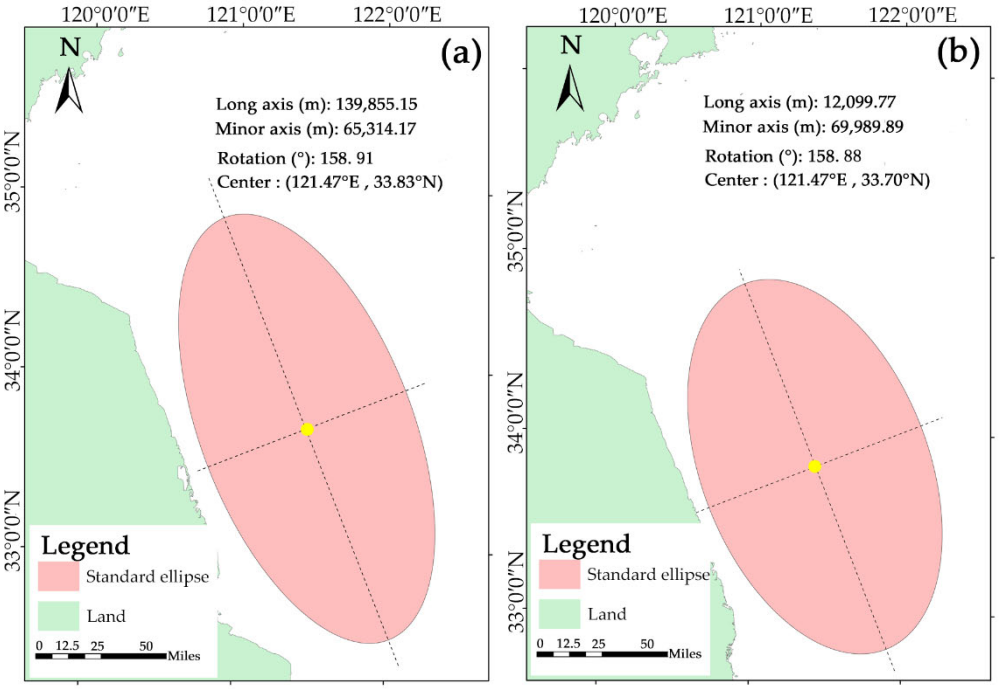


FIGURE 9. Standard deviational ellipses of the experimental results and of the reference data: (a) shows the ellipse for the experimental results and (b) shows the ellipse for the reference data.

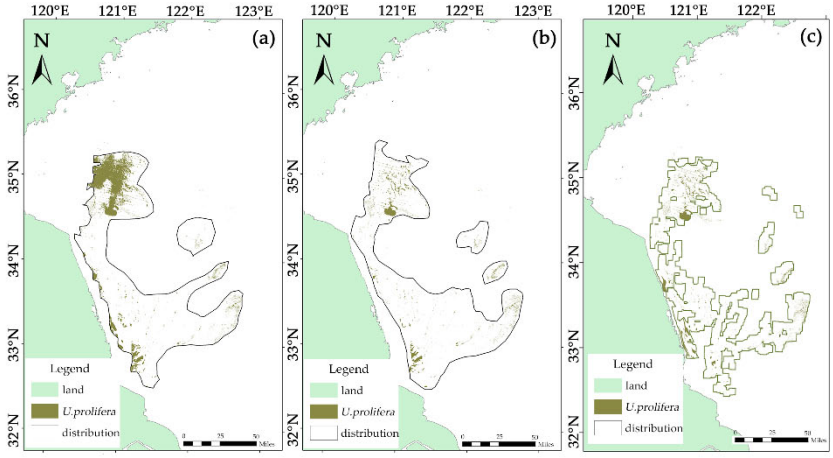


FIGURE 10. *U. prolifera* coverage area extracted from only one source: (a) shows the *U. prolifera* coverage area extracted using only MODIS images, (b) shows the *U. prolifera* coverage area extracted using only sentinel-2A images and(c)shows the results from the paper.

In Fig. 10a the *U. prolifera* coverage area is 348.73 km^2. Compared with the results of this study and that reported by the SOA, the *U. prolifera* coverage area is overestimated in Fig. 10a due to the 250-m-resolution. About 23% of the *U. prolifera* coverage area in the figure overlaps the results of this study and those reported by the SOA, which means that MODIS has the advantage of estimating *U. prolifera* over a large sea area, but its estimation accuracy in local areas needs to be improved.

In Fig. 10b, the *U. prolifera* coverage area is 80.50 km^2. Due to the 10-m-resolution of the Sentinel-2A images, the results in this case are closer to the results reported by the SOA and our methods. Here as well, the northernmost point of the *U. prolifera* distribution is inaccurate because of the lack of surveillance ship data. In Fig. 10b, about 12% of the pixels are not consistent with the reference data, which could be attributed to a lack of other vegetation index data (e.g. RVI, FAI and DVI).

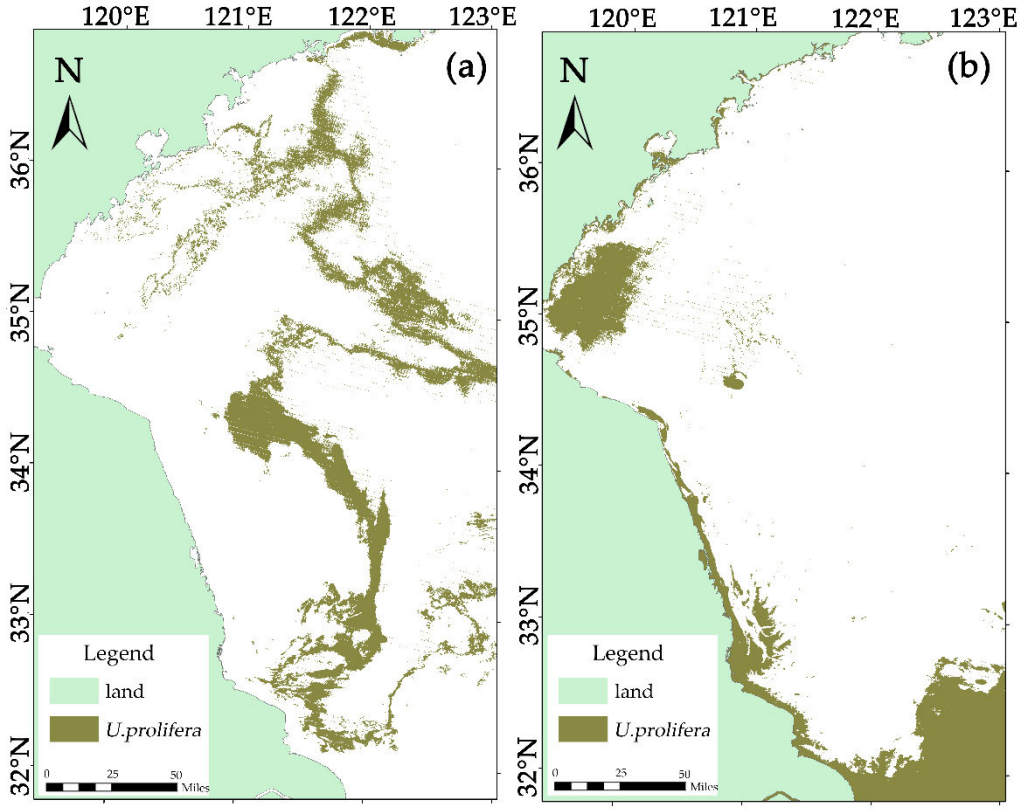


FIGURE 11. ***U. prolifera*** **coverage area extracted using other algorithms: (a) shows** ***U. prolifera*** **coverage area extracted using the maximum-likelihood supervised classification, and (b) shows the** ***U. prolifera*** **coverage area extracted using the minimum-distance supervised classification.**

Although the results from only Sentinel-2A images is closer to the reference data, it does not meet the requirements for a daily map of *U. prolifera* due to the visit cycle of Sentinel-2A.

E. COMPARING EXPERIMENTAL RESULTS WITH THOSE OBTAINED USING SUPERVISED METHODS.

In this section, comparisons of the improved method with the maximum likelihood supervised classification [41] and minimum supervised classification [42] are shown. Maximum likelihood supervised classification takes into account the variance-covariance within the class distributions, for normally distributed data, and has better performance than other known parametric classifiers [41]. Minimum distance classification works well when there is a low variability between the classes and classes are distinct [43]. Because of these properties, the two classification methods are commonly used in land classification using RS images.

To apply these two algorithms, the surveillance ship data were first processed into binary images and merged with MODIS and Sentinel-2A images. Second, this study chose a 100 pixels covered by *U. prolifera* as visual interpretation training data for the two algorithms, according to the SOA's reference data. Then, the two algorithms were run in ENVI4.8. In this paper, the two algorithms will not be described in detail. Fig. 11 shows the *U. prolifera* coverage area extracted using the two algorithms.

In Fig. 11, the coverage area extracted using the minimum-distance method is 27120.75 km^2 and that extracted using the maximum-likelihood method is 159021.81 km^2. The results extracted from our improved method and those reported by the SOA are both covered by the results of the two algorithms. The *U. prolifera* coverage area extracted from the two algorithms is therefore overestimated and many pixels with cloud and land are included. Therefore, it can be concluded that the improved method may be better than the two algorithms.

IV. CONCLUSION

The timely and effective detection of *U. prolifera* in the Yellow Sea can considerably benefit water transportation, the ecology, and the economy of the coastal areas. The daily detection of *U. prolifera* using MODIS and Sentinel-2A satellite images or SAR images from individual sources presents challenges in terms of timeliness and effectiveness. The surveillance ship data in the local area are powerful for validating the existence of *U. prolifera*. However, this source falls short in terms achieving a balance between low cost and good area coverage. Combining remote sensing data and surveillance ship data is a promising approach for the daily monitoring of *U. prolifera* in the Yellow Sea. However, there

is a lack of methods that can automatically detect *U. prolifera* coverage and distribution while making full use of data from multiple sources.

To address this issue, based on MODIS images with 250-meter resolution, Sentinel-2A images with 10-meter resolution, and surveillance ship data, a D-S-evidence-based data fusion approach is proposed here as an improved method to determine the coverage area and distribution of *U. prolifera*. Comparison with reference data from the SOA showed that the results from our proposed method were correct in terms of spatial position and morphological characteristics. A comparison between the results from the fusion of multi-source data and those from individual data sources demonstrated that the proposed method is advantageous in terms of the spatial distribution and coverage area, making it highly beneficial for daily and emergent monitoring tasks pertaining to *U. prolifera*.

Further study on *U. prolifera* detection could proceed in the following directions: (i) obtain more data for detecting *U. prolifera*, such as UAV data, data from volunteers, and SAR images, to use in modifying this method, particularly for cloudy weather; (ii) incorporate more characteristics of *U. prolifera*, such as the TM greenness after tassel transformation and image texture features, for more effective detection; and (iii) use objective-based algorithms to extract the *U. prolifera* coverage with high accuracy based on RS images.

REFERENCES

[1] T. W. Cui, X. J. Liang, C. Tong, Y. F. Xiao, R. J. Liu, X. Zhang, and J. Zhang, "Assessing and refining the satellite-derived massive green macro-algal coverage in the Yellow Sea with high resolution images," *ISPRS J. Photogramm. Remote Sens.*, vol. 144, pp. 315–324, Oct. 2018.

[2] V. Smetacek and A. Zingone, "Green and golden seaweed tides on the rise," *Nature*, vol. 504, no. 7478, pp. 84–88, 2013.

[3] Q. Xing and C. Hu, "Mapping macroalgal Blooms in the Yellow Sea and East China Sea using HJ-1 and Landsat data: Application of a virtual baseline reflectance height technique," *Remote Sens. Environ.*, vol. 178, pp. 113–126, Jun. 2016.

[4] C. Hu and M.-X. He, "Origin and offshore extent of floating algae in Olympic sailing area," *Eos, Trans. Amer. Geophys. Union*, vol. 89, no. 33, pp. 302–303, Aug. 2008.

[5] D. A. Lyons, C. Arvanitidis, A. J. Blight, E. Chatzinikolaou, T. Guy-Haim, J. Kotta, H. Orav-Kotta, A. M. Queirós, G. Rilov, P. J. Somerfield, and T. P. Crowe, "Macroalgal Blooms alter community structure and primary productivity in marine ecosystems," *Global Change Biol.*, vol. 20, no. 9, pp. 2712–2724, 2014.

[6] N.-H. Ye, X.-W. Zhang, Y.-Z. Mao, C.-W. Liang, D. Xu, J. Zou, Z.-M. Zhuang, and Q.-Y. Wang, "'Green tides' are overwhelming the coastline of our blue planet: Taking the world's largest example," *Ecological Res.*, vol. 26, no. 3, pp. 477–485, 2011.

[7] X. Gu, X.-F. Chen, Q. Yin, Z.-Q. Li, H. Xu, Y. Shao, and Z.-W. Li, "Stereoscopic remote sensing used in monitoring enteromorpha prolifra disaster in Chinese yellow sea," *Spectrosc. Spectral Anal.*, vol. 31, no. 6, pp. 1627–1632, 2011.

[8] W. Shang, Z. Gao, X. Jiang, C. Liu, and W. Gao, "Green tide disaster monitoring system based on multi-source data," in *Proc. SPIE Opt. Eng. Appl.*, San Diego, CA, USA, 2016, Art. no. 99750O.

[9] Y. Cao, Y. Wu, Z. Fang, X. Cui, J. Liang, and X. Song, "Spatiotemporal patterns and morphological characteristics of *Ulva prolifera* distribution in the Yellow Sea, China in 2016–2018," *Remote Sens.*, vol. 11, no. 4, p. 445, 2019.

[10] X. Liu, Z. Wang, and X. Zhang, "A review of the green tides in the Yellow Sea, China," *Marine Environ. Res.*, vol. 119, pp. 189–196, Aug. 2016.

[11] Y. B. Son, B.-J. Choi, Y. H. Kim, and Y.-G. Park, "Tracing floating green algae blooms in the Yellow Sea and the East China Sea using GOCI satellite data and Lagrangian transport simulations," *Remote Sens. Environ.*, vol. 156, pp. 21–33, Jan. 2015.

[12] C. Hu, "A novel ocean color index to detect floating algae in the global oceans," *Remote Sens. Environ.*, vol. 113, pp. 2118–2129, Oct. 2009.

[13] W. Shi and M. Wang, "Green macroalgae Blooms in the Yellow Sea during the spring and summer of 2008," *J. Geophys. Res.*, vol. 114, no. C12, Dec. 2009, Art. no. C12010.

[14] M. Wang and C. Hu, "Mapping and quantifying *Sargassum* distribution and coverage in the Central West Atlantic using MODIS observations," *Remote Sens. Environ.*, vol. 183, pp. 350–367, Sep. 2016.

[15] B. Liu, E. J. D'Sa, and I. Joshi, "Sa, and I. Joshi, "Multi-decadal trends and influences on dissolved organic carbon distribution in the Barataria Basin, Louisiana from *in-situ* and Landsat/MODIS observations," *Remote Sens. Environ.*, vol. 228, pp. 183–202, Jul. 2019.

[16] R. A. Araya-López, J. Lopatin, F. E. Fassnacht, and H. J. Hernández, "Monitoring Andean high altitude wetlands in central Chile with seasonal optical data: A comparison between Worldview-2 and Sentinel-2 imagery," *ISPRS J. Photogram. Remote Sens.*, vol. 145, pp. 213–224, Nov. 2018.

[17] P. J. Zarco-Tejada, A. Hornero, R. Hernández-Clemente, and P. S. A. Beck, "Understanding the temporal dimension of the red-edge spectral region for forest decline detection using high-resolution hyperspectral and Sentinel-2a imagery," *ISPRS J. Photogram. Remote Sens.*, vol. 137, pp. 134–148, Mar. 2018.

[18] M. P. Ferreira, F. H. Wagner, L. E. O. C. Aragão, Y. E. Shimabukuro, and C. R. de Souza Filho, "Tree species classification in tropical forests using visible to shortwave infrared WorldView-3 images and texture analysis," *ISPRS J. Photogram. Remote Sens.*, vol. 149, pp. 119–131, Mar. 2019.

[19] L. H. S. Rotta, D. R. Mishra, F. S. Y. Watanabe, T. W. P. Rodrigues, E. H. Alcântara, and N. N. Imai, "Analyzing the feasibility of a space-borne sensor (SPOT-6) to estimate the height of submerged aquatic vegetation (SAV) in inland waters," *ISPRS J. Photogram. Remote Sens.*, vol. 144, pp. 341–356, Oct. 2018.

[20] T.-W. Cui, J. Zhang, L.-E. Sun, Y.-J. Jia, W. Zhao, Z.-L. Wang, and J.-M. Meng, "Satellite monitoring of massive green macroalgae Bloom (GMB): Imaging ability comparison of multi-source data and drifting velocity estimation," *Int. J. Remote Sens.*, vol. 33, no. 13, pp. 5513–5527, 2012.

[21] X. Fan and Y. Liu, "A global study of NDVI difference among moderate-resolution satellite sensors," *ISPRS J. Photogramm. Remote Sens.*, vol. 121, pp. 177–191, Nov. 2016.

[22] R. K. Gupta, S. Prasad, T. S. V. Nadham, and G. H. Rao, "Relative sensitivity of district mean RVI and NDVI over an agrometeorological zone," *Adv. Space Res.*, vol. 13, no. 5, pp. 261–264, 1993.

[23] H. Yuan, C. Wu, L. Lu, and X. Wang, "A new algorithm predicting the end of growth at five evergreen conifer forests based on nighttime temperature and the enhanced vegetation index," *ISPRS J. Photogram. Remote Sens.*, vol. 144, pp. 390–399, Oct. 2018.

[24] Q. Xing, L. Wu, L. Tian, T. Cui, L. Li, F. Kong, X. Gao, and M. Wu, "Remote sensing of early-stage green tide in the Yellow Sea for floating-macroalgae collecting campaign," *Mar. Pollut. Bull.*, vol. 133, pp. 150–156, Aug. 2018.

[25] J. W. Rouse, R. H. Haas, J. A. Schell, and D. W. Deering, "Monitoring vegetation systems in the great plains with ERTS," in *Proc. 3rd ERTS Symp.*, 1973.

[26] Y. Xiao, "Remote sensing estimation of the biomass of floating *Ulva prolifera* and analysis of the main factors driving the interannual variability of the biomass in the Yellow Sea," *Mar. Pollut. Bull.*, vol. 140, pp. 330–340, Mar. 2019.

[27] X. Cai, T. Cui, R. Zheng, P. Qin, and B. Mu, "Comparison of algorithms for green macro-algae Bloom detection based on geostationary ocean color imager," *Remote Sens.*, vol. 29, no. 5, pp. 44–50, 2014.

[28] A. P. Dempster, "Upper and lower probabilities induced by a multivalued mapping," *Ann. Math. Statist.*, vol. 38, no. 2, pp. 325–339, Apr. 1967.

[29] P. Diaconis and G. Shafer, "A mathematical theory of evidence," *J. Amer. Stat. Assoc.*, vol. 73, no. 363, p. 677, Sep. 1978.

[30] Z. Fang, Y. Jiang, H. Xu, S.-L. Shaw, L. Li, and X. Geng, "An invisible salient landmark approach to locating pedestrians for predesigned business card route of pedestrian navigation," *Sensors*, vol. 18, no. 9, p. 3164, 2018.

[31] Y. Zhou, Z. Fang, Q. Li, and S. Guo, "Anomalous taxi trajectory detection based on experiential constraint rules and evidence theory," *Geomatics Inf. Sci. Wuhan Univers*, vol. 41, no. 6, pp. 797–802, 2016.

[32] R. R. Yager, "On the Dempster-Shafer framework and new combination rules," *Inf. Sci.*, vol. 41, no. 2, pp. 93–137, Mar. 1987.

[33] C. K. Murphy, "Combining belief functions when evidence conflicts," *Decis. Support Syst.*, vol. 29, no. 1, pp. 1–9, Jul. 2000.
[34] M. B. Hisham, S. N. Yaakob, R. A. A. Raof, A. B. A. Nazren, and N. M. Wafi, "An analysis of performance for commonly used interpolation method," *Adv. Sci. Lett.*, vol. 23, no. 6, pp. 5147–5150, Jun. 2017.
[35] A. Shaker, W. Y. Yan, and P. E. LaRocque, "Automatic land-water classification using multispectral airborne LiDAR data for near-shore and river environments," *ISPRS J. Photogramm. Remote Sens.*, vol. 152, pp. 94–108, Jun. 2019.
[36] D. Reynolds, "Gaussian mixture models," in *Encyclopedia Biometrics*, S. Z. Li and A. K. Jain, Eds. Boston, MA, USA: Springer, 2015, pp. 827–832.
[37] F. Xiao, "Multi-sensor data fusion based on the belief divergence measure of evidences and the belief entropy," *Inf. Fusion*, vol. 46, pp. 23–32, Mar. 2019.
[38] V. Kumar, A. Sharma, R. Bhardwaj, and A. K. Thukral, "Comparison of different reflectance indices for vegetation analysis using Landsat-TM data," *Remote Sens. Appl., Soc. Environ.*, vol. 12, pp. 70–77, Nov. 2018.
[39] L. Li, D. Ma, C. Wang, and X. Gu, "New method for conflict evidence processing in D-S theory," *Appl. Res. Comput.*, vol. 28, no. 12, pp. 4528–4531, 2011.
[40] J. Hu *et al.*, "An improving image boundary tracking algorithm based on eight neighborhood," *Bull. Surv. Mapping*, vol. 12, no. 12, pp. 21–25, 2018.
[41] M. A. Bowers and S. F. Matter, "Landscape ecology of mammals: Relationships between density and patch size," *J. Mammalogy*, vol. 78, no. 4, pp. 999–1013, 1997.
[42] R. B. Whitlatch, A. H. Hines, S. F. Thrush, J. E. Hewitt, and V. Cummings, "Benthic faunal responses to variations in patch density and patch size of a suspension-feeding bivalve," *J. Exp. Mar. Biol. Ecology*, vol. 216, nos. 1–2, pp. 171–189, 1997.
[43] J. Wu, *Landscape Ecology: Pattern Process Scale and Grade*. Beijing, China: Higher Education, 2000.



ZHONGYUAN WANG is currently pursuing the M.S. degree with the State Key Laboratory for Information Engineering in Surveying, Cartography and Geographical Information Engineering, Wuhan University. His research interests include data fusion and algorithm study.



ZHIXIANG FANG received the M.Sc. and Ph.D. degrees from Wuhan University, in 2002 and 2005, respectively, where he is currently a Professor with the State Key Laboratory for Information Engineering in Surveying, Mapping and Remote Sensing. His research interests include spatiotemporal modeling of human behavior, space-time GIS for transport, and intelligent navigation.



YICHEN WU is currently pursuing the M.S. degree with the State Key Laboratory for Information Engineering in Surveying, Cartography and Geographical Information Engineering, Wuhan University. Her research interests include data mining and exploration with big data.



JIANFENG LIANG received the M.S. degree from Nankai University. He is currently an Engineer with National Marine Data and Information Service, China. His research interests include marine data storage management technology, cloud computing technology, and big data technology.



XIAO SONG received the M.S. degree from Chang'an University, in 2012. She is currently an Engineer with National Marine Data and Information Service, China. Her researche interests include system design and development, marine big data technology, and virtual machine technology.